Enhanced performance of a biomimetic membrane for Na2CO3 crystallization in the scenario of CO2 capture

Ye, Wenyuan; Lin, Jiuyang; Tækker Madsen, Henrik; Gydesen Søgaard, Erik; Hélix-Nielsen, Claus; Luis, Patricia; Van der Bruggen, Bart

Published in:
Journal of Membrane Science

Link to article, DOI:
10.1016/j.memsci.2015.09.010

Publication date:
2016

Document Version
Peer reviewed version

Enhanced performance of a biomimetic membrane for Na_2CO_3 crystallization in the scenario of CO_2 capture

Highlights

- Aquaporin based FO membrane was applied as membrane crystallizer to crystallize Na_2CO_3
- High water flux and low reverse salt flux can be realized by using this biomimetic membrane
- $Na_2CO_3 \cdot 10H_2O$ crystals with a purity of 99.94% can be achieved
- Negligible membrane fouling and membrane blockage were observed

Graphical Abstract:

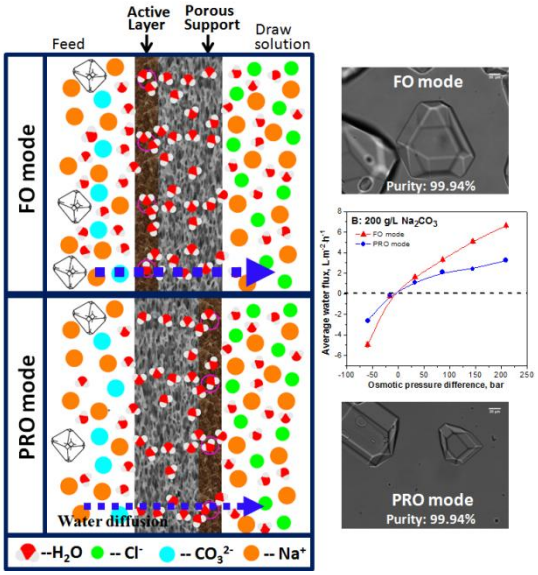

Enhanced performance of a biomimetic membrane for Na_2CO_3 crystallization in the scenario of CO_2 capture

Wenyuan Ye[a], Jiuyang Lin[a]*, Henrik Tækker Madsen[b], Erik Gydesen Søgaard[b], Claus Hélix-Nielsen[c,d], Patricia Luis[e], Bart Van der Bruggen[a]

* Corresponding author. E-mail: jiuyanglin4@gmail.com

[a] *Department of Chemical Engineering, KU Leuven, Willem de Croylaan 46, B-3001 Heverlee, Belgium*

[b] *Department of Biotechnology, Chemistry and Environmental Engineering, Aalborg University, Niels BohrsVej 8, 6700 Esbjerg, Denmark*

[c] *Aquaporin A/S, Ole MaaløesVej 3, DK-2200 Copenhagen N, Denmark*

[d] *The biomimetic membrane group, Department of Environmental Engineering, Technical University of Denmark, DK-2800 KongensLyngby, Denmark*

[e] *Materials & Process Engineering (iMMC-IMAP), Université catholique de Louvain, Place Sainte Barbe 2, 1348 Louvain-la-Neuve, Belgium*

Abstract: Membrane assisted crystallization (MACr) offers an innovative platform for crystallizing Na_2CO_3, allowing its reuse after CO_2 capture from flue gases by an alkaline solution (*i.e.*, NaOH). In this study, the biomimetic Aquaporin Inside™ membrane AIM60 was employed to enhance water removal, facilitating Na_2CO_3 crystallization. The water channel in the active layer, comprising aquaporin proteins, and the strong wettability of membrane substrate assist a better performance. The AIM60 membrane water flux in forward osmosis (FO) mode was 6.62 $L \cdot m^{-2} \cdot h^{-1}$ and 3.25 $L \cdot m^{-2} \cdot h^{-1}$ in pressure retarded osmosis (PRO) mode. In comparison, a dense reverse osmosis membrane yielded 0.21 $L \cdot m^{-2} \cdot h^{-1}$ in FO mode and 0.16 $L \cdot m^{-2} \cdot h^{-1}$ in PRO mode, and a porous hydrophobic membrane in a membrane contactor yielded a flux of 0.08 $L \cdot m^{-2} \cdot h^{-1}$.

Crystallization utilizing the AIM 60 membrane in an osmotic crystallizer was achieved without noticeable membrane scaling or degradation. Furthermore, a proper control of the supersaturation level induces crystallization of $Na_2CO_3 \cdot 10H_2O$ crystals with a purity of 99.94%. Hence, the Aquaporin Inside™ FO membrane may be a promising alternative to existing methods for Na_2CO_3 crystallization for its application in a CO_2 capture scenario.

Keywords: Biomimetic aquaporin membranes, CO_2 capture scenario, Membrane crystallization, Forward osmosis

1. Introduction

Crystallization is a versatile method for separation and purification to produce a wide range of products in the chemical industry [1], such as pharmaceuticals, additives, pigments, fine chemicals, etc. Most of these products are marketed in crystalline form, requiring a high purity and specific polymorphism [2]. However, current conventional techniques, such as vapor diffusion by evaporation, seeding, and anti-solvent extraction, have some disadvantages that influence the production efficiency and the crystalline quality [3]. The main challenge is that the quality of the obtained crystals is poorly reproducible, which is ascribed to a poorly controlled supersaturation, defective mixing, heterogeneous distribution of solvent removal or anti-solvent addition points over the plant [3].

Generally, crystallization occurs due to a local concentration gradient and the dynamics of creating supersaturation for crystal nucleation and growth in a crystallizer. The level of local supersaturation directly governs the crystal morphology, structure, and purity [4]. These properties influence the quality of the products. Additionally, downstream processes, such as filtration, drying, compaction as well as storage, are dependent on the crystal morphology. However, excessive supersaturation may yield impure crystals with inclusions, unsteady modifications, needle-like shape and small particles [4]. Thus, in order to generate high-quality crystals, precise control of the supersaturation is required.

A new crystallization technique, based on membrane technology - membrane assisted crystallization (MACr), is emerging as an innovative technique to meet the

requirements in crystallization. With MACr, one can better control and limit the maximum level of supersaturation due to its well-defined mass transfer through the membrane, resulting in a favorable crystal size, shape and purity [4, 5], Simultaneously, the membrane promotes heterogeneous nucleation, which in turn reduces the induction time (defined as the time passed between reaching supersaturation and the formation of crystals) of the crystallization process [6]. Membrane crystallization outperforms conventional techniques (*i.e.*, cooling or evaporation), due to the fact that it can be conducted at room temperature, or at mildly elevated temperature using waste heat or alternative energy sources (*i.e.*, solar energy or geothermal energy) [7, 8]. To date, the use of membranes has been regarded as a "process intensification" strategy to satisfy the requirements of sustainable development [9, 10]. MACr has broadened its potential applications in recent years, such as the production of pharmaceuticals or proteins or their recovery from waste streams [11-15], as well as valuable resource recovery from high salinity streams [16-22]. For instance, Caridi *et al.* [23] and Profio *et al.* [24] employed a hydrophobic hollow fiber membrane module in osmotic membrane distillation for separation of proteins, allowing the crystallization of pure proteins with a uniform size and specific polymorphism at room temperature. Luis *et al.* [25] demonstrated that osmotic membrane distillation has the potential for production of $Na_2CO_3 \cdot 10H_2O$ crystals from CO_2-rich solutions for closing the loop of CO_2 sequestration. Ye *et al.* [26] further investigated the effect of inorganic impurities on the Na_2CO_3 crystallization in view of a realistic scenario of CO_2 capture, demonstrating that crystals with ca. 99.5%

purity can be obtained with the exclusion of co-crystals of impurities. However, osmotic membrane distillation, with an inherently low driving force (arising from the transmembrane vapor pressure gradient), fails to provide high mass transfer: ca. 0.09 to 0.18 $kg \cdot m^{-2} \cdot h^{-1}$ at room temperature [25-27]. To promote the mass transfer through hydrophobic membranes, thermally assisted membrane distillation is an interesting solution at elevated temperatures [19, 28, 29]. However, the requirement of superhydrophobicity (contact angles > 150°) [30] to effectively prevent membrane wetting still seems to be a challenge in this approach [31, 32].

Alternatively, a dense hydrophilic membrane, *i.e.*, reverse osmosis (RO) membrane, in an osmotic membrane crystallizer has been proven to possess a better performance for dewatering, producing highly ordered crystals at room temperature, compared to osmotic membrane distillation [33-35]. In this crystallizer, the hydrophilic membrane allows the water transfer by liquid diffusion rather than by vapor diffusion. An improvement of mass transfer by nearly one order of magnitude, from 0.65 to 1.70 $kg \cdot m^{-2} \cdot h^{-1}$, can be achieved [35]. Inevitably, the dewatering rate for the dense hydrophilic membrane is still insufficient compared to thermally assisted membrane crystallization, which would involve a larger membrane area and an increase of the investment cost [19, 36-39].

A newly developed biomimetic aquaporin forward osmosis (FO) membrane may solve these issues when employed in a membrane crystallizer. This type of FO membrane comprises highly selective water channel proteins so-called aquaporins. Aquaporins have single channel turnover rates of up to 10^9 water molecules per

second, facilitating gradient driven water diffusion while blocking salt permeation and several membrane designs have been suggested in recent reviews [40, 41].

In this work, the potential of biomimetic FO membranes was studied to crystallize Na_2CO_3 in a CO_2 capture scenario using a membrane crystallizer equipped with an Aquaporin FO membrane (AIM 60). The AIM 60 membrane was characterized in order to explore its feasibility for Na_2CO_3 crystallization by investigating membrane stability and mass transfer mechanism, and the properties of the obtained crystals were subsequently studied.

2. Materials and methods

2.1 Materials

Anhydrous Na_2CO_3 salt (analytical grade) was supplied by VWR (Belgium) to simulate the alkaline solution obtained from CO_2 capture by NaOH. NaCl with 99.9% purity was supplied by VWR (Belgium) and applied as the draw solution throughout the experiments. Ultrapure water with a conductivity of 18.2 $M\Omega \cdot cm^{-1}$ (Millipore Mili-Q, Billerica, MA) was used throughout the experiments. The AIM 60 FO membrane from Aquaporin Inside^{TM} (Denmark) was applied in a lab-made osmosis membrane crystallizer. The specifications of the AIM 60 FO membrane as reported by the manufacturer are shown in Table 1.

Table 1 Specification of the Aquaporin flat sheet FO membrane

Specifications	
Water flux	＞ 7 $L \cdot m^{-2} \cdot h^{-1}$ (H_2O vs 1M NaCl; FO mode)
NaCl reverse flux	＜2 $g \cdot m^{-2} \cdot h^{-1}$ (H_2O vs 1M NaCl; FO mode)
Operating conditions	Temperature range: 5-50 ^oC (Short term exposure: 65 ^oC)
	pH limit: 2-11

2.2 Experimental setup

A schematic diagram of the setup for osmotic crystallization is shown in Figure 1. The AIM 60 FO membrane separates the mother solution of Na_2CO_3 from the osmotic solution flow (*i.e.*, NaCl) under isothermal conditions. The hydrophilic nature of the membrane allows the transfer of water between the Na_2CO_3 solution and NaCl solution by diffusion. Two peristaltic pumps (Watson Marlow 313 and Watson Marlow 323E/D, UK) were used to circulate the feed and stripping stream from the cylindrical glasses to the membrane crystallizer in the same current direction. The feed solutions were circulated at a constant flow rate of 2.5 $L \cdot h^{-1}$ and the osmotic solution was circulated at 3.13 $L \cdot h^{-1}$. Co-current flow was used to reduce the strain on the membrane surface.

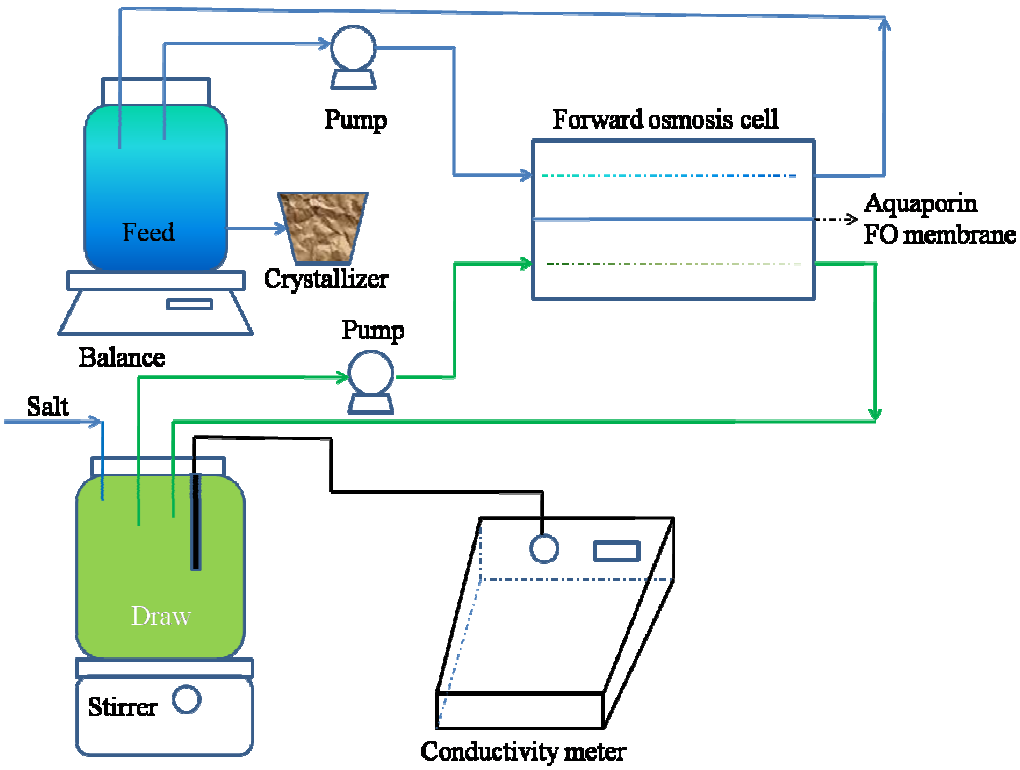

Fig. 1 Schematic diagram of the bench-scale FO unit for Na_2CO_3 crystallization

Utilizing an osmotic crystallizer to obtain Na_2CO_3 crystals with high quality, namely, a good morphology, high purity, and a uniform XRD pattern, two different membrane orientations were explored to investigate the penetration of salts (NaCl and Na_2CO_3) through osmotic permeability measurements. The preferable mode operates at lower reverse salt diffusion. When the draw solution (*i.e.*, NaCl or Na_2CO_3) flows on the support layer side of the membrane, and the deionized water flows along the active layer side, this is denoted as FO mode. Conversely, when the draw solution contacts the active side of membrane and the pure water faces the back side layer, it is denoted as pressure retarded osmosis (PRO) mode. Osmotic flux data were collected for NaCl concentrations ranging from 100 to 250 $g \cdot L^{-1}$. The concentrations of the

Na_2CO_3 solution used as the feed solutions ranged from 50 to 200 $g \cdot L^{-1}$. The temperature of both solutions was maintained at room temperature (20 ± 1 °C).

The feed solution composed of Na_2CO_3 as the target component with different initial concentrations (100 $g \cdot L^{-1}$ to 200 $g \cdot L^{-1}$) was drawn by different concentrations of stripping solutions to assess the water flux in FO as well as PRO mode. Higher water transfer is preferable for more efficiently concentrating Na_2CO_3. The conductivity of the draw solution was measured and a constant concentration throughout the experiments was maintained by dosing with NaCl salt. The draw solution was continuously stirred with a magnetic mixer (Fisher Scientific, Belgium) at 300 rpm to ensure a homogeneous concentration.

Furthermore, to identify the optimal membrane orientation for Na_2CO_3 crystallization, the process for concentrating Na_2CO_3 solution was studied in different operating modes (FO vs PRO). The experiment was continued until crystals were observed in the feed solution; the obtained crystals were characterized immediately by microscopy, according to the procedure described in section 2.4.2.

Membrane stability was determined by measuring the water flux for concentrating Na_2CO_3 solution in alternation operated at a preferable mode. The feed solution was concentrated to its nucleation point and then replaced by a fresh 200 $g \cdot L^{-1}$ Na_2CO_3 solution for next cycle. Five repetitions of this crystallization process were conducted. After that, the pure water flux and salt permeability were determined to investigate the possibility of membrane blockage/damage. The characteristics of the used membrane were detected by scanning electron microscopy (SEM), as described in Section 2.4.1.

In addition, several pieces of the AIM 60 membrane were immersed into a salt solution for 7 days to assess their stability. 50 $g \cdot L^{-1}$ and 300 $g \cdot L^{-1}$ NaCl as well as 50 $g \cdot L^{-1}$ Na_2CO_3 solutions were applied as the soaking solutions to simulate the working environment for the biomimetic membranes.

2.3 Water flux and reverse solute flux determination

The experimental water flux was calculated by measuring the weight difference of the feed solution, and recorded by a digital scale with an accuracy of +/-0.01 g. Since the experiments were conducted in batch, the water flux gradually decreases with the increased concentration of the feed solution or with the dilution of the draw solution. The flux is calculated by the weight difference versus time, using the following equation:

$$J_W = -\frac{\Delta m_{water}}{\rho_s \cdot A \cdot \Delta t} \quad (1)$$

where Δm_{water} is the total mass decrease of permeate water from the feed solution to the draw solution over a predetermined time Δt, ρ_s is the density of solutions at room temperature, and A is the membrane area (4.91×10^{-4} m^2). When the system remained stable, data were collected at the interval of 5 minutes during 30 minutes for one batch to test the pure water flux and reverse salt flux. Mean value of these 6 data collections was calculated to evaluate the membrane performance. Due to the short testing period, the salt permeability is negligible. Thus, ρ_s is equal to the water density.

The reverse solute flux (J_s) of Na_2CO_3 or NaCl was determined by the transfer of salt from the salt solution to the pure water as follows:

$$J_s = \frac{V_t \cdot C_t - V_0 \cdot C_0}{A \cdot t} \quad (2)$$

where C_t and V_t is the concentration and volume of Na_2CO_3 or NaCl in the pure water as a feed solution measured at time t, respectively. C_0 and V_0 is the initial concentration and volume of the solute in feed solution, respectively.

Due to the fact that a certain amount of salts transferred through the membrane to the opposite side, the mass difference of reversed NaCl and Na_2CO_3 salts should be considered for the calculation of Δm_{water} in Eq. 1 for the calculation of water flux when concentrating Na_2CO_3 by using NaCl as draw solution.

$$\Delta m_{water} = (m_{t_i} - m_{t_{i+1}}) + (\Delta m_{NaCl,\,P} - \Delta m_{Na_2CO_3,P}) \quad (3)$$

where m_{t_i} and $m_{t_{i+1}}$ is the total mass of feed solution at time t_i and t_{i+1}, respectively. $\Delta m_{NaCl,\,P}$ is the mass of reversed NaCl salt to the Na_2CO_3 side and $\Delta m_{Na2CO3,\,P}$ is the mass of reversed Na_2CO_3 salt to the NaCl side.

The mass of reversed salts, $\Delta m_{s,\,P}$, (*i.e.*, NaCl or Na_2CO_3) can be calculated by Eq. 4:

$$\Delta m_{s,\,P} = J_s \cdot A \cdot t \quad (4)$$

where J_s is the reverse solute flux, A is the membrane area, and t is the operating time.

2.4 Analytical methods

2.4.1 Characterization of membranes

Contact angle measurements were performed with a Drop Shape Analysis System DSA 10 Mk2 (Krüss, Germany) to determine the hydrophobicity of the AIM 60 membrane. The surface and inner topology of the original and used Aquaporin

membranes were explored by scanning electron microscopy (SEM), using an accelerating voltage of 10.0 kV at different magnifications. The membrane samples were dried in a vacuum chamber, then fractured in liquid nitrogen and sputtered with gold nanoparticles for the cross-section SEM measurement.

2.4.2 Characterization of crystals

The properties of crystal samples were characterized by ion chromatography, microscopy, X-ray diffraction (XRD), and total water fraction (TWF), as described elsewhere [26, 35].

3. Results and discussion

3.1 Membrane morphology

In the biomimetic AIM 60 membrane, aquaporin proteins incorporated in the membrane structure can potentially facilitate gradient driven water diffusion in FO process [42]. In order to investigate how the membrane morphology is potentially affected by the crystallization process, the basic membrane morphology is characterized (see Figs. 2, 3, and 4).

As shown in Fig. 2, the AIM FO membrane has substrate with a thickness of ~109 µm. Specifically, the substrate has an open-cell sponge-like structure with inter-connecting pores, resulting in high porosity as indicated in Fig. 3. In addition, some macrovoids with a pore diameter on the order of several hundred nanometers are well developed at the bottom of the substrate. This structure is well suited for

enhancing the wettability of the membrane substrate, mitigating the concentration polarization phenomenon and thus promoting water transfer [43-48].

As observed in Fig. 4, the AIM 60 FO membrane has a selective polyamide layer with a thickness of ~200 nm in which Aquaporin containing vesicles are embedded. The vesicles appear well dispersed in the top layer of the membrane. However, some defects were observed on the membrane surface, triggering the risk of salt leakage during FO. Fig. 5 shows the anticipated pathways for mass transfer in the AIM membrane on the basis of the membrane design [40, 49].

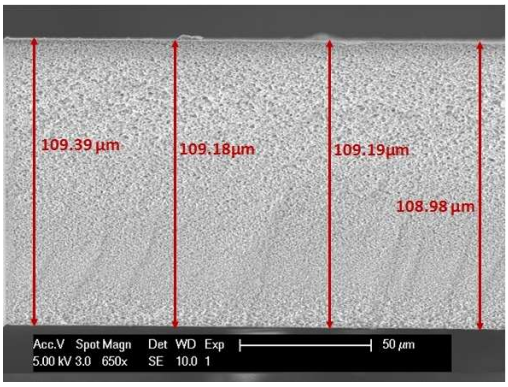

Fig. 2 Overall cross-section SEM image of the AIM 60 FO membrane

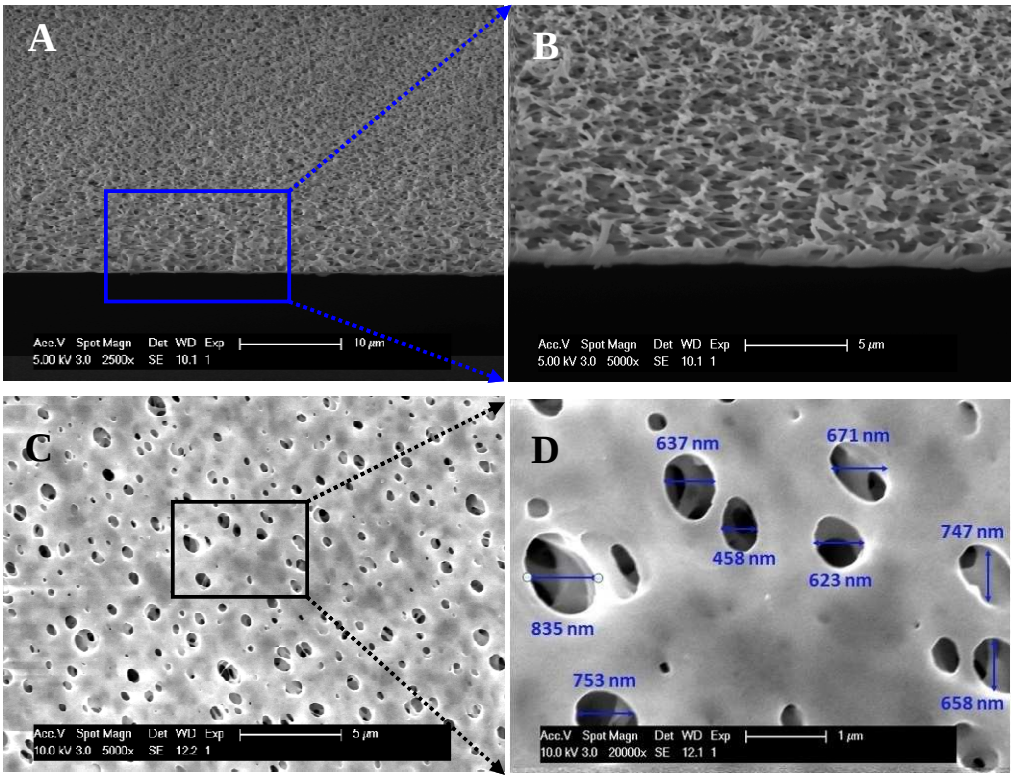

Fig. 3 SEM images of the AIM 60 membrane substrate. (A, B) Cross section for the support layer side at 2500× and 5000×, respectively; (C, D) Support surface at 5000× and 20000×, respectively

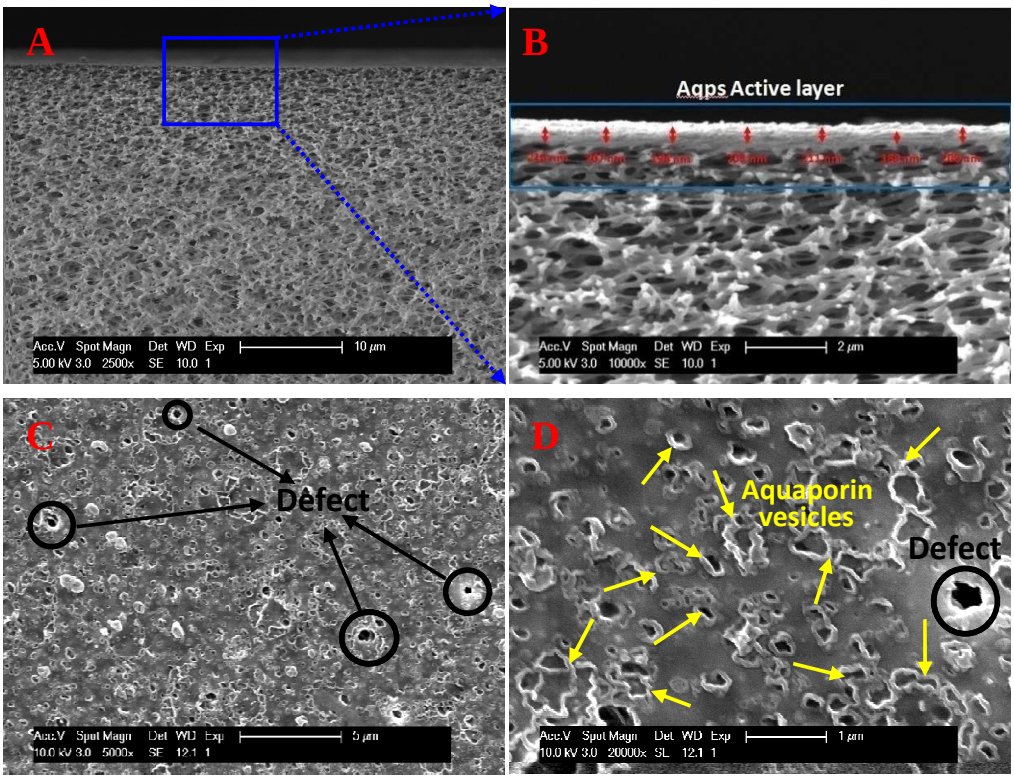

Fig. 4 SEM images of active surface of the AIM 60 membrane. (A, B) Cross section of active layer at 2500× and 10000×, respectively; (C, D) Active layer surface at 5000× and 20000×, respectively

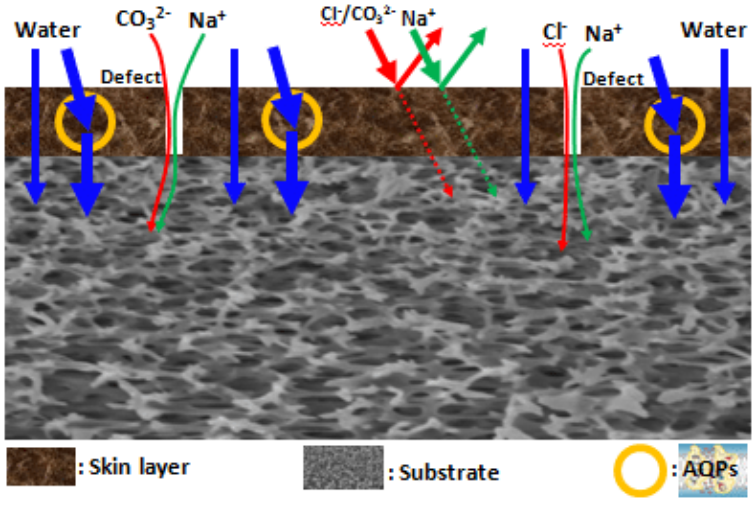

Fig. 5 Schematic of mass transfer in the AIM 60 FO membrane (see Ref. [40])

3.2 Hydrophilicity assessment

Fig. 6 shows the hydrophilicity of the AIM 60 membrane as a function of contact time. The selective layer of this FO membrane is strongly hydrophilic, with a static contact angle of 41.5° (see Fig. 6). The contact angle on the AIM 60 membrane surface reduces gradually from 41.5° to 37.2° within the measurement time. This indicates that the water transfer is enhanced through the membrane due to the presence of aquaporin protein vessels in active layer. As for the support layer of the AIM 60 membrane, the large pore size allows a fast water penetration through the membrane to contact with the selective layer for water transfer. The contact angle measurement of the back layer of the membrane is shown in Supplementary video.

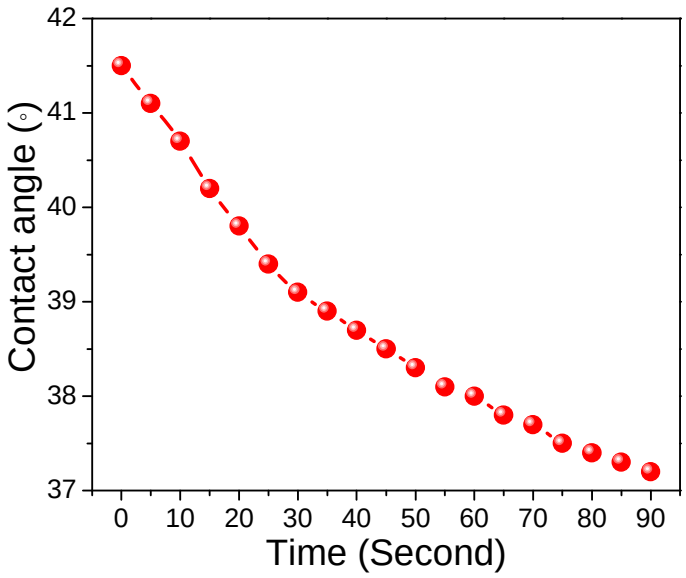

Fig. 6 Contact angles of the active layer of AIM 60 membrane as a function of time

3.3 Membrane performance

3.3.1 Pure water flux and salt rejection of the biomimetic membrane

The role of the membrane in osmotic crystallization is to provide sufficient mass transfer as well as to avoid impurities (*i.e.*, NaCl) in the crystalline Na_2CO_3. Therefore, the mass transfer performance in terms of pure water flux and reverse solute flux of two different membrane orientations (FO or PRO mode) was systematically studied to investigate the suitability of the AIM 60 membrane for crystallization (see Fig. 7).

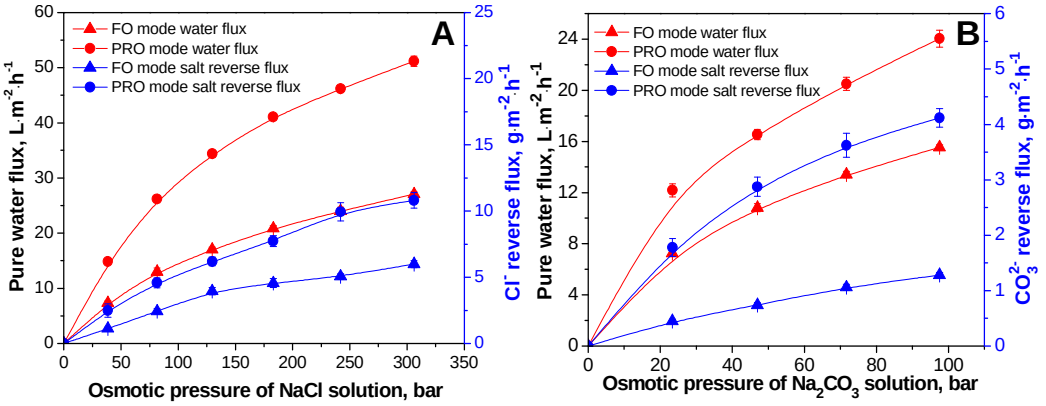

Fig.7 Pure water flux and salt reverse flux at different concentration of stripping solution in different operating modes (FO mode: pure water facing active layer with salt solution at support layer side; PRO mode: salt facing active layer with pure water at the backing membrane side. A: NaCl; B: Na_2CO_3)

As illustrated in Fig. 7, the permeate flux is enhanced by a higher solute concentration in both operating modes due to the higher driving force resulting from the higher osmotic pressure difference between salt solution and pure water. The water flux displays a nonlinear increase with the transmembrane osmotic pressure. This is attributed to internal concentration polarization, which has been demonstrated in previous studies [46, 50, 51].

In addition, the presence of an electrostatic barrier in aquaporin proteins can hamper ion transport [52, 53]. Consequently, the biomimetic FO membrane should have a low reverse salt flux. As indicated in Fig. 7, the salt permeation flux, recorded as 1.12 ± 0.12 $g \cdot m^{-2} \cdot h^{-1}$ in FO mode driven by 50 $g \cdot L^{-1}$ NaCl, is consistent with the value provided by the manufacturer in Table 1. This is comparable to the HTI CTA membrane (ca. 1.23 $g \cdot m^{-2} \cdot h^{-1}$ in FO mode with 58.5 $g \cdot L^{-1}$ NaCl as draw solution) and lower than that for the HTI thin film composite (TFC) membranes (ca. 4.45 $g \cdot m^{-2} \cdot h^{-1}$ in FO mode with 58.5 $g \cdot L^{-1}$ NaCl as draw solution) [54]. However, the AIM 60 membrane performed better in PRO mode in terms of salt permeation, 2.48 ± 0.51 $g \cdot m^{-2} \cdot h^{-1}$ salt permeability at 50 $g \cdot L^{-1}$ NaCl, compared to HTI CTA membrane with ca. 7.67 $g \cdot m^{-2} \cdot h^{-1}$ salt diffusion flux and HTI TFC membrane with ca. 9.54 $g \cdot m^{-2} \cdot h^{-1}$ at 58.5 $g \cdot L^{-1}$ NaCl [54]. It is noteworthy that rather low reverse salt flux in PRO membrane performance is obtained with existing defects on the membrane surface (see Fig. 4). Presumably, the performance may be better if the number of defects is minimized.

As indicated in Fig. 7, the water flux of AIM 60 membrane is dependent on the osmotic pressure differences between pure water and draw solutions, regardless of the solute type (Na_2CO_3 or NaCl) and the membrane orientation. However, the reverse CO_3^{2-} flux for the Aquaporin membrane is slightly lower than the reverse Cl^- flux. This is mainly due to the charge repulsion effect of the Aquaporin membrane, which is demonstrated in other studies [55, 56]. Furthermore, due to the specific morphology of the AIM 60 membrane, regardless of the salt species, a higher salt permeation is

obtained when the salt contacts the active layer of the membrane. Conversely, when the salt is in contact with the support layer, less salt can penetrate to the opposite side.

3.3.2 Dehydration of Na_2CO_3 solution by osmotic crystallizer

The AIM 60 FO membrane was used both in FO and PRO mode for dehydration of a Na_2CO_3 solution with different concentrations to further ensure the optimal membrane orientation for efficiently crystallizing Na_2CO_3. The water flux as a function of time interval under different osmotic pressure differences in different operating modes is shown in Supplementary Fig. S1. It can be seen that the transmembrane flux has a slightly decreasing trend as a function of operation time. This is attributed to the moderate depletion of the driving force across the membrane because of the concentration of the Na_2CO_3 solutions.

Fig. 8 shows the average flux as a function of the osmotic pressure difference for different processing modes. Unexpectedly, the water permeated more slowly in PRO mode than in FO mode. This is presumably due to the fact that more NaCl diffused to the feed side in PRO mode and then the effective osmotic pressure in the stripping solution was depreciated so that the osmotic pressure in the feed solution was enhanced. In this case, the water transfer from the feed side to the stripping part can be limited by a lower driving force. However, in FO mode, a certain amount of Na_2CO_3 migrated to the NaCl side. This induced an increase of the osmotic pressure in the draw solute but a decline of the osmotic pressure in the feed liquor, enhancing the driving force for water transport across the membrane.

Generally, a nonlinear increase of the transmembrane flux with the increase of the osmotic pressure difference is observed as shown in Fig. 8. This can be explained in terms of the enhancement of internal concentration polarization at a higher salt concentration. However, a substantial water flux can still be achieved. The mean water flux was 6.62 $L \cdot m^{-2} \cdot h^{-1}$ for concentrating Na_2CO_3 with 200 $g \cdot L^{-1}$ stripped by 300 $g \cdot L^{-1}$ NaCl solution in FO mode, which is one to two orders of magnitude higher than that in previous studies [26, 35]. This impressive performance of the AIM 60 FO membrane in terms of water transport is promising for application in membrane crystallization.

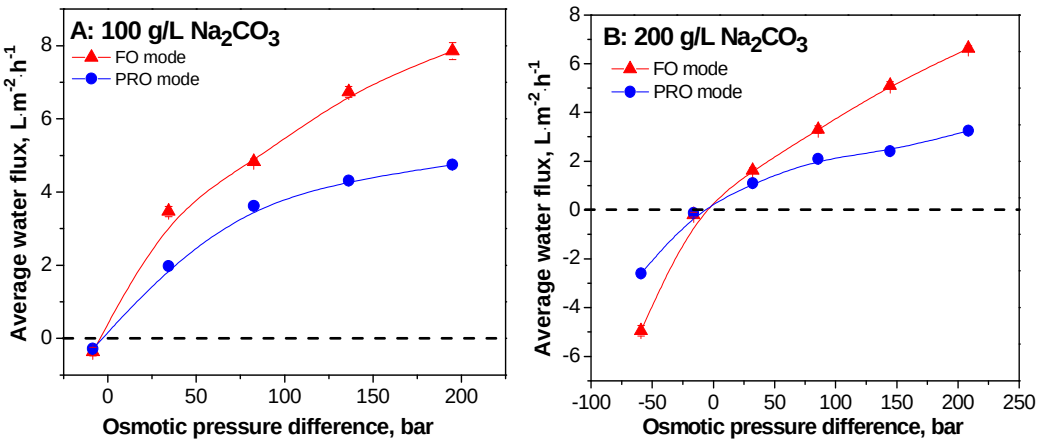

Fig. 8 Average water flux as a function of osmotic pressure difference across the membrane when operated in FO and PRO modes

3.3.3 Crystallization performance

Fig. 9 illustrates the dewatering performance of the AIM 60 FO membrane for Na_2CO_3 crystallization. As observed in Fig. 9, a slight decline of the water flux

occurred in the initial period at both operating modes. This was caused by a reduced driving force across the membrane, which was triggered by the dewatering of Na_2CO_3 mother liquor. Subsequently, the water flux leveled off when the feed side reached its supersaturation status since a steady osmotic pressure difference between feed and draw solutes was achieved after reaching the targeted supersaturation. Compared to asymmetric reverse osmosis membranes (*i.e.*, BW30, Dow Film Tec) [35], the AIM 60 FO membrane presented a better performance because of its superior water flux. Thus, the AIM 60 membrane crystallizer can produce crystals in a more efficient way, which in turn saves membrane areas for this production process. Furthermore, the FO mode provides a more efficient mass transfer than PRO mode, which is consistent with the results in Section 3.3.2. Thus, FO mode is the optimal choice for Na_2CO_3 crystallization by using an AIM membrane in a crystallizer.

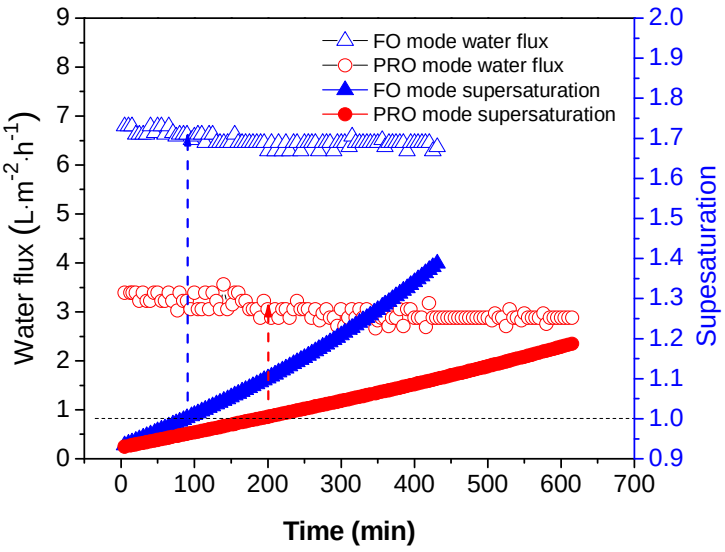

Fig. 9 Performance of Aquaporin FO membranein Na_2CO_3crystallization

3.4 Crystal characterization

3.4.1 Crystalline microstructure

Fig. 10 shows the micrographs of the formed crystals from both FO and PRO modes at 20× and 10× magnifications. As observed from Fig. 10A and C, orderly polyhedral monocrystals of Na_2CO_3 were generated in both operation modes. As shown in Fig. 10B and D, small crystals (marked with dash dot circles) aggregated on the surface of grown crystals. Simultaneously, growing crystals (indicated by solid circles) bundled to adjacent counterparts due to the limited space for crystal growth in the crystallizer. As illustrated in Fig. 10B and D, the majority of the crystals have a highly organized form, except for a minority of aggregated crystals. This indicates that the AIM 60 membrane can act as an effective physical barrier for a well-controlled supersaturation environment, which allows Na_2CO_3 crystals to grow regularly and controllably [2, 57].

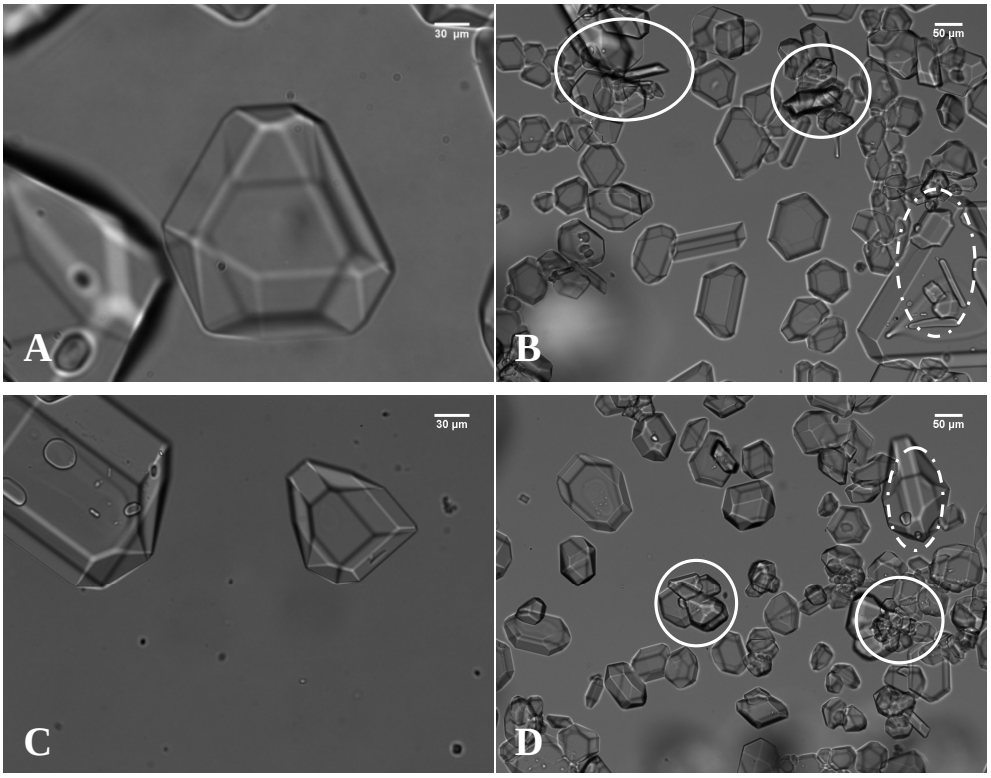

Fig. 10 Microscopy images of obtained crystals. (A, B) Crystals from FO mode at 20× and 10×, respectively; (C, D) Crystals from PRO mode at 20× and 10×, respectively

3.4.2 Crystalline pattern determination

Generally, three crystalline forms, *i.e.*, $Na_2CO_3 \cdot 10H_2O$, $Na_2CO_3 \cdot 7H_2O$, and $Na_2CO_3 \cdot H_2O$, can be generated from aqueous Na_2CO_3 solution under different thermodynamic conditions. Therefore, further investigation of the crystalline pattern of obtained crystals by XRD and TWF measurements is of interest, and this is shown in Fig. 11 and Table 2.

As shown in Fig. 11, $Na_2CO_3 \cdot 10H_2O$ is the main form of the generated crystals in both FO and PRO mode. This can be further demonstrated by TWF measurement (Table 2). The crystals originated from FO mode have a water fraction of 62.87 ±

0.11%, and 62.86 ± 0.12% in PRO mode. These data are consistent with the theoretical water fraction of 62.94% for $Na_2CO_3 \cdot 10H_2O$ crystals.

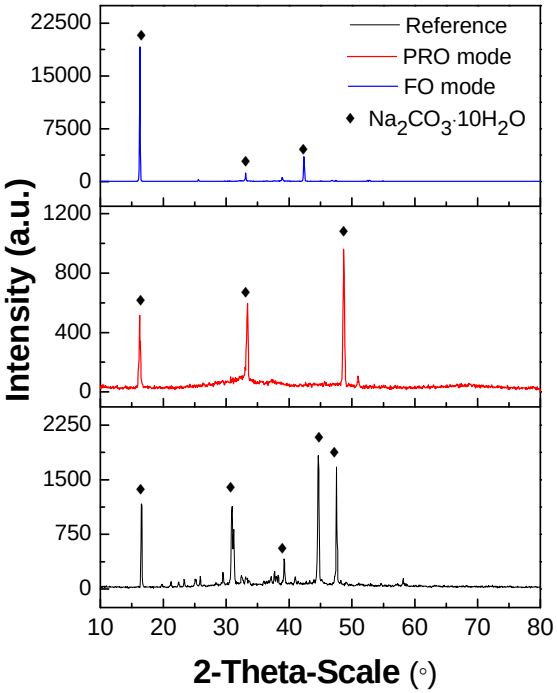

Fig. 11 XRD patterns of the obtained crystals from different operating modes

Additionally, crystals obtained with the AIM FO membrane crystallizer have the same polymorphism as the crystals generated in previous work [26, 35], reflecting the fact that the obtained crystals were formed under similar thermodynamic conditions, namely, <30% Na_2CO_3 mother liquor at room temperature [26]. Theoretically, the crystalline structure of Na_2CO_3 crystal in aqueous solution is mainly influenced by the temperature and the concentration of Na_2CO_3 in the mother liquid, as the evident from the phase diagram for the thermodynamic formation of Na_2CO_3 [58]. The

concentration of Na_2CO_3 ranging from 32.0 to 45.7% within a range of temperatures between 32.5 and 35.4 °C leads to the production of $Na_2CO_3 \cdot 7H_2O$. Higher concentrations in the mother liquid of Na_2CO_3 result in the formation of binary mixture of $Na_2CO_3 \cdot 10H_2O/Na_2CO_3 \cdot 7H_2O$ or $Na_2CO_3 \cdot 7H_2O/Na_2CO_3 \cdot H_2O$. This implies that by a proper control of the supersaturation level of the mother solutions, specific target crystalline forms of the polymorphic crystals can be achieved.

3.4.3 Purity of the produced crystals

As indicated in Table 2, 0.59 $g \cdot kg^{-1}$ Cl^- is contained in the crystals from AIM membrane crystallizer in FO mode, while crystals generated from PRO mode have a slightly higher Cl^- content, *i.e.*, 0.60 $g \cdot kg^{-1}$. Compared to the crystals from other processes, the Cl^- content in crystals obtained in this work is higher than that generated by a membrane contactor with 0.24 $g \cdot kg^{-1}$ Cl^- [26] and an RO membrane crystallizer (0.09 $g \cdot kg^{-1}$ in FO mode and 0.14 $g \cdot kg^{-1}$ in PRO mode) [35]. Due to the defects in the surface of the AIM membrane, more Cl^- passes through the Aquaporin membrane than through the hydrophobic hollow fibers or the dense RO membrane. Hence, a higher amount of Cl^- in the target mother liquor tends to lower the purity of Na_2CO_3 crystals. However, the concentration of Cl^- contained in crystals (0.06%) in this study is still much lower than that in Na_2CO_3 generated by the Solvay method (*i.e.*, 0.15% of Cl^-) [59]. The purity of the generated crystals with the AIM membranes reaches 99.94%, which is pure enough for industrial application, such as in the glass industry [59].

Table 2 Properties of the Na_2CO_3 obtained by different approaches

Sample		Total water fraction (%)	Cl^- content ($g \cdot kg^{-1}$)/ Na_2CO_3 purity (%)	Ref.
Theoretical value	$Na_2CO_3 \cdot 10H_2O$	62.94	-	-
	$Na_2CO_3 \cdot 7H_2O$	54.31	-	-
	$Na_2CO_3 \cdot H_2O$	14.52	-	-
Membrane contactor	Direct contact mode	62.96 ± 0.22	0.24/99.98	[26]
BW 30 membrane	FO mode	62.84 ± 0.18	0.09/99.99	[35]
	PRO mode	62.84 ± 0.23	0.14/99.99	[35]
Aquaporin membrane	FO mode	62.87 ± 0.11	0.59/99.94	This work
	PRO mode	62.86 ± 0.12	0.60/99.94	This work
Solvey method	Na_2CO_3	-	1.50/99.85	[59]

3.5 Membrane stability

In the crystallization process, the AIM membranes were applied in a rather harsh environment (*i.e.*, high salinity and high pH). Specifically, the AIM membrane was used with a high salinity of draw solution with 300 $g \cdot L^{-1}$ NaCl and a target solution of Na_2CO_3 at a concentration near or above supersaturation (215 $g \cdot L^{-1}$ Na_2CO_3 at 20 ^oC). In order to be applicable in long-term industrial process with the AIM membranes, the investigation of the membrane stability is essential for its potential long-term performance, as presented in Figs. 12-15.

SEM images of the membranes after immersion into different kinds of salts with different concentrations for 7 days are shown in Fig. 12. The surfaces of the membranes in different salts with different concentrations are almost identical to the

pristine surface in Fig. 2. Even in 300 $g \cdot L^{-1}$ NaCl solution, the surface of the membrane remains the same. This demonstrates the feasibility of using AIM membranes in osmotic crystallization driven by a high salinity draw solution.

The stability of the AIM membrane was assessed by repeating crystallization processes in terms of water flux through the membrane (see Fig. 13). Fig. 13 shows that the membrane performance is steady over five cycles. The mass transfer remains considerably consistent with the increase of cycle time. This indicates that the fouling propensity for the AIM membrane in this application is negligible. The absence of a sharp decline of the water flux within each cycle proves that no significant membrane fouling or damage occurs during the crystallization process with a proper control of the supersaturation for the target solutions.

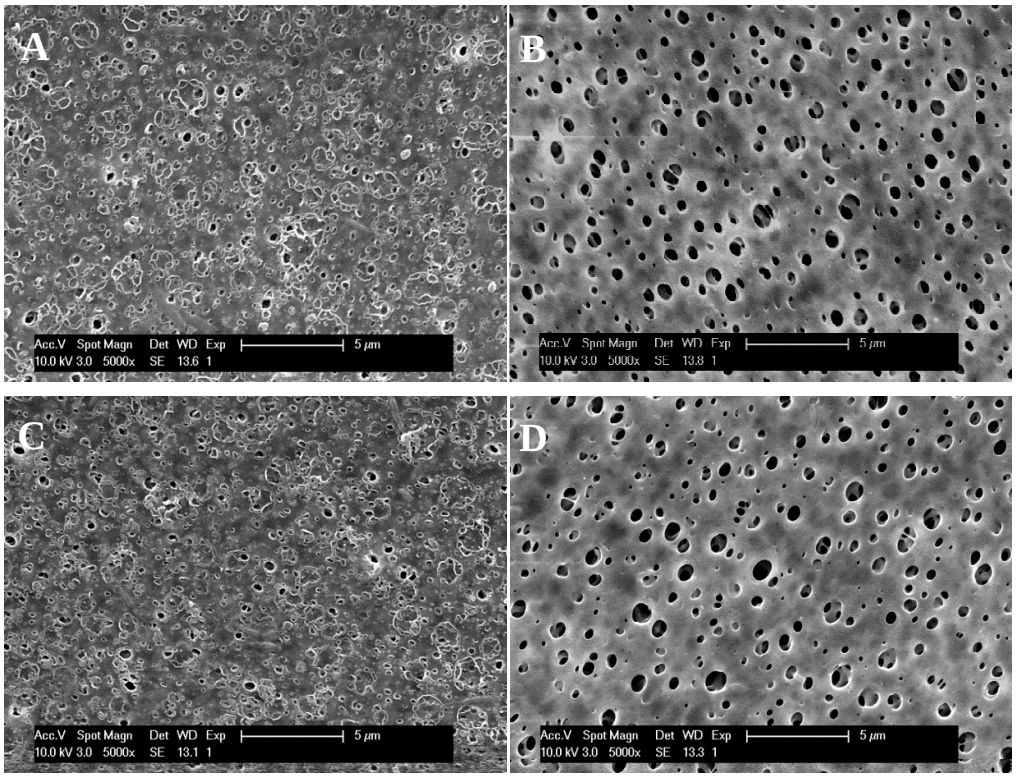

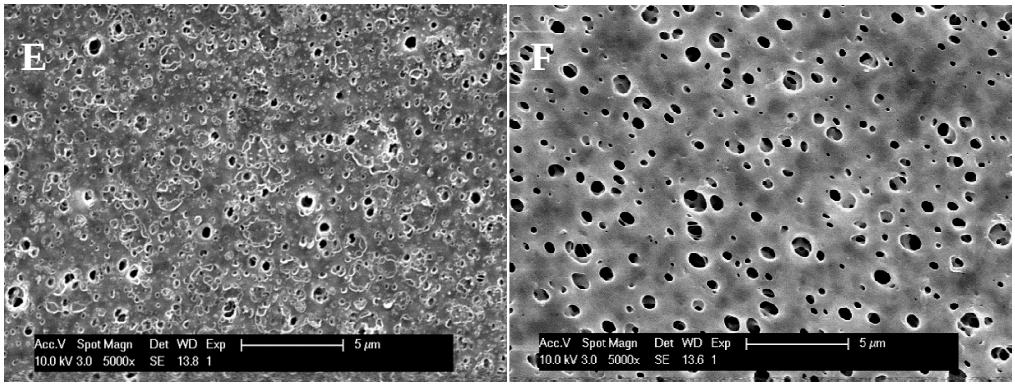

Fig. 12 SEM images of the membranes immersed in salt solutes for 7 days at 5000×. (A, B) Active and support surface of membranes in 50 $g \cdot L^{-1}$ NaCl, respectively; (C, D) Active and support surface of membranes in 300 $g \cdot L^{-1}$ NaCl, respectively; (E, F) Active and support surface of membranes in 50 $g \cdot L^{-1}$ Na_2CO_3, respectively.

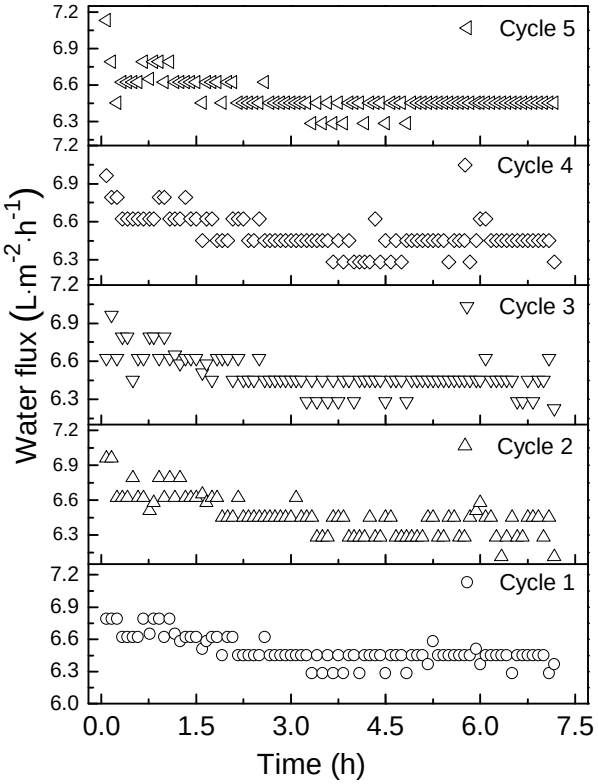

Fig. 13 Cycling performance of Aquaporin membrane for Na_2CO_3 crystallization.

To further investigate membrane scaling, the used AIM membranes for Na_2CO_3 crystallization were investigated by SEM measurement, which is indicated in Fig. 14. Compared to the pristine membrane in Figs. 3 and 4, no apparent differences between the original membrane and the applied membrane can be seen. Furthermore, no fouling or scaling was observed on the membrane surface after five crystallization cycles as shown in Fig. 14A and B. The cross section images of the applied membranes in Fig. 14C, D, and E also indicate that no crystals grew inside the pores.

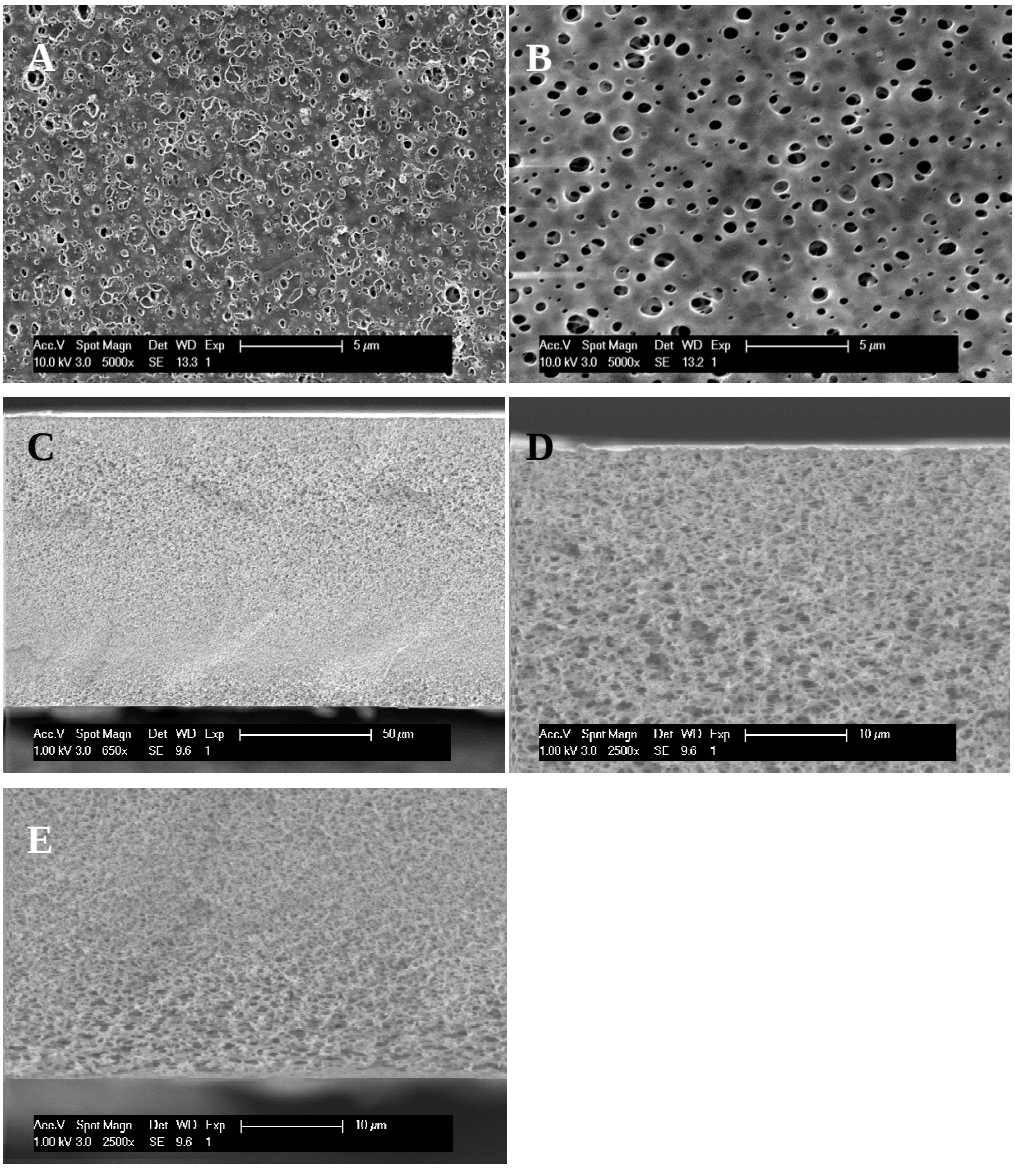

Fig. 14 SEM images of the membranes after crystallization. (A) Active surface at 5000×; (B) Support layer at 5000×. (C) Cross section of the membrane at 350×; (D) Cross section for the active layer side at 2500×; (E) Cross section for the support layer side at 2500×.

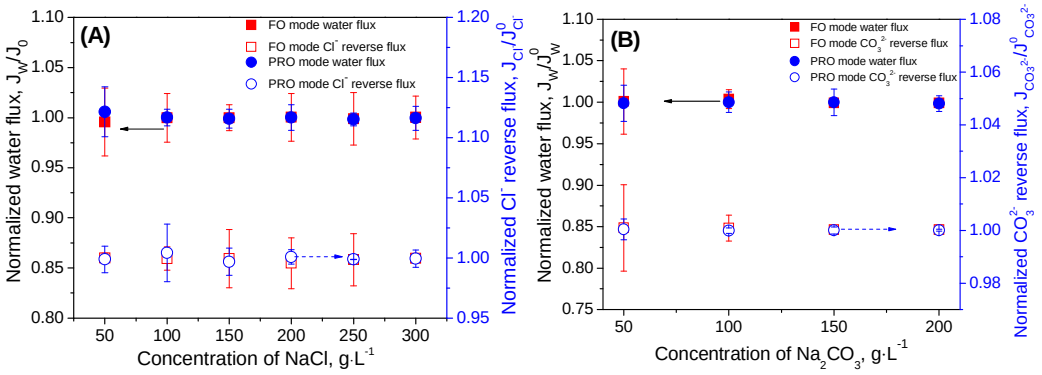

Fig. 15 Comparison of the performance of applied Aquaporin membranes after crystallization to original Aquaporin membranes in term of water flux and salt reverse flux. (A) NaCl; (B): Na_2CO_3.

Finally, the applied membranes were investigated in terms of their mass transfer. Fig. 15 indicates that the ratios of water flux and salt reverse flux for the applied membrane to the original membrane values are around 1.0 within the range of statistical uncertainty, regardless of the species of salts and membrane orientation. This confirms that no membrane damage or fouling occurs during crystallization. Therefore, the AIM membrane can be indeed applied under the harsh combined conditions of high salinity and high pH in supersaturated Na_2CO_3 solutions.

4. Conclusion

In this work, a biomimetic Aquaporin FO membrane was successfully employed for crystallization of Na_2CO_3, in view of CO_2 capture. The typical water channel with enbedded Aquaporin proteins can enhance the transmembrane water flux. Regardless of the membrane orientation for crystallization, boththe water flux and salt diffusion were promoted by the increase of the draw solution concentration. However, FO mode was a better alternative than PRO mode to crystallize Na_2CO_3 due to its higher water permeation flux and lower unexpected salt diffusion.

Through the crystallization process, it is demonstrated that by applying this biomimetic FO membrane in a membrane crystallizer, good performance can be obtained with no apparent membrane scaling or blockage. The crystallizer equipped with AIM 60membrane can control the supersaturation rate of the target solution, resulting in the production of $Na_2CO_3 \cdot 10H_2O$ with a purity of 99.94%. The mean water flux was >6 $L \cdot m^{-2} \cdot h^{-1}$ for concentrating Na_2CO_3 with 200 $g \cdot L^{-1}$ stripped by 300 $g \cdot L^{-1}$ NaCl solution in FO mode, which is one to two orders of magnitude higher than other Na_2CO_3 crystallization approaches (*i.e.*, membrane contactor and dense reverse osmosis membrane crystallizer). In conclusion, the biomimetic FO membrane constitutes a potential alternative to the existing methods for membrane crystallization.

Acknowledgements

Wenyuan Ye and Jiuyang Lin thank the support provided by China Scholarship

Council of the Ministry of Education, P. R. China. Michele Vanroelen from CIT, KU Leuven, is acknowledged for assisting the performance on the ion chromatography. Claus Hélix-Nielsen was supported by a grant from the Danish National Advanced Technology Foundation (Grant No.: 97-2012-4).

References

[1] A. Myerson, Handbook of industrial crystallization, Butterworth-Heinemann, 2002.

[2] E. Drioli, G. Di Profio, E. Curcio, Progress in membrane crystallization, Curr. Opin. Chem. Eng., 1 (2012) 178-182.

[3] N.S. Tavare, Micromixing limits in an MSMPR crystallizer, Chem. Eng. Technol., 12 (1989) 1-11.

[4] D. Weckesser, A. König, Particle shape and purity in membrane based crystallization, Chem. Eng. Technol., 31 (2008) 157-162.

[5] C. Charcosset, A review of membrane processes and renewable energies for desalination, Desalination, 245 (2009) 214-231.

[6] E. Curcio, S. Simone, G.D. Profio, E. Drioli, A. Cassetta, D. Lamba, Membrane crystallization of lysozyme under forced solution flow, J. Membr. Sci., 257 (2005) 134-143.

[7] F. Macedonio, E. Drioli, E. Curcio, G. Di Profio, Experimental and economical evaluation of a membrane crystallizer plant, Desalin. Water Treat., 9 (2009) 49-53.

[8] E. Drioli, E. Curcio, G. Di Profio, F. Macedonio, A. Criscuoli, Integrating

membrane contactors technology and pressure-driven membrane operations for seawater desalination: energy, exergy and costs analysis, Chem. Eng. Res. Des., 84 (2006) 209-220.

[9] T. Van Gerven, A. Stankiewicz, Structure, energy, synergy, time - The fundamentals of process intensification, Ind. Eng. Chem. Res., 48 (2009) 2465-2474.

[10] R. Kumar, D. Vikramachakravarthi, P. Pal, Production and purification of glutamic acid: A critical review towards process intensification, Chem. Eng. Process., 81 (2014) 59-71.

[11] Y. Wu, Y. Kong, J. Liu, J. Zhang, J. Xu, An experimental study on membrane distillation-crystallization for treating waste water in taurine production, Desalination, 80 (1991) 235-242.

[12] G. Di Profio, E. Curcio, E. Drioli, Trypsin crystallization by membrane-based techniques, J. Struct. Biol., 150 (2005) 41-49.

[13] G. Di Profio, C. Stabile, A. Caridi, E. Curcio, E. Drioli, Antisolvent membrane crystallization of pharmaceutical compounds, J. Pharm. Sci., 98 (2009) 4902-4913.

[14] M. Brito Martínez, N. Jullok, Z. Rodríguez Negrín, B. Van der Bruggen, P. Luis, Membrane crystallization for the recovery of a pharmaceutical compound from waste streams, Chem. Eng. Res. Des., 92 (2014) 264-272.

[15] E. Curcio, G. Di Profio, E. Drioli, Recovery of fumaric acid by membrane crystallization in the production of L-malic acid, Sep. Purif. Technol., 33 (2003) 63-73.

[16] F. Edwie, T.-S. Chung, Development of hollow fiber membranes for water and

salt recovery from highly concentrated brine via direct contact membrane distillation and crystallization, J. Membr. Sci., 421 (2012) 111-123.

[17] G. Chen, Y. Lu, W.B. Krantz, R. Wang, A.G. Fane, Optimization of operating conditions for a continuous membrane distillation crystallization process with zero salty water discharge, J. Membr. Sci., 450 (2014) 1-11.

[18] L. Martinez-Diez, F. Florido-Diaz, Desalination of brines by membrane distillation, Desalination, 137 (2001) 267-273.

[19] C.M. Tun, A.G. Fane, J.T. Matheickal, R. Sheikholeslami, Membrane distillation crystallization of concentrated salts—flux and crystal formation, J. Membr. Sci., 257 (2005) 144-155.

[20] R. Creusen, J. van Medevoort, M. Roelands, A. van Renesse van Duivenbode, J.H. Hanemaaijer, R. van Leerdam, Integrated membrane distillation–crystallization: Process design and cost estimations for seawater treatment and fluxes of single salt solutions, Desalination, 323 (2013) 8-16.

[21] F. Edwie, T.-S. Chung, Development of simultaneous membrane distillation–crystallization (SMDC) technology for treatment of saturated brine, Chem. Eng. Sci., 98 (2013) 160-172.

[22] G. Chen, Y. Lu, X. Yang, R. Wang, A.G. Fane, Quantitative Study on Crystallization-Induced Scaling in High-Concentration Direct-Contact Membrane Distillation, Ind. Eng. Chem. Res., 53 (2014) 15656-15666.

[23] A. Caridi, G. Di Profio, R. Caliandro, A. Guagliardi, E. Curcio, E. Drioli, Selecting the desired solid form by membrane crystallizers: crystals or cocrystals,

Cryst. Growth Des., 12 (2012) 4349-4356.

[24] G.D. Profio, A. Caridi, R. Caliandro, A. Guagliardi, E. Curcio, E. Drioli, Fine dosage of antisolvent in the crystallization of l-histidine: Effect on polymorphism, Cryst. Growth Des., 10 (2009) 449-455.

[25] P. Luis, D. Van Aubel, B. Van der Bruggen, Technical viability and exergy analysis of membrane crystallization: Closing the loop of CO_2 sequestration, Int. J. Greenh. Gas Control, 12 (2013) 450-459.

[26] W. Ye, J. Lin, J. Shen, P. Luis, B. Van der Bruggen, Membrane crystallization of sodium carbonate for carbon dioxide recovery: Effect of impurities on the crystal morphology, Cryst. Growth Des., 13 (2013) 2362-2372.

[27] M.B. Martínez, N. Jullok, Z.R. Negrín, B. Van der Bruggen, P. Luis, Membrane crystallization for the recovery of a pharmaceutical compound from waste streams, Chem. Eng. Res. Des., 92 (2014) 264-272.

[28] S. Meng, Y. Ye, J. Mansouri, V. Chen, Crystallization behavior of salts during membrane distillation with hydrophobic and superhydrophobic capillary membranes, J. Membr. Sci., 473 (2015) 165-176.

[29] K.L. Hickenbottom, T.Y. Cath, Sustainable operation of membrane distillation for enhancement of mineral recovery from hypersaline solutions, J. Membr. Sci., 454 (2014) 426-435.

[30] L. Feng, S. Li, Y. Li, H. Li, L. Zhang, J. Zhai, Y. Song, B. Liu, L. Jiang, D. Zhu, Super□hydrophobic surfaces: from natural to artificial, Adv. Mater., 14 (2002) 1857-1860.

[31] A. Razmjou, E. Arifin, G. Dong, J. Mansouri, V. Chen, Superhydrophobic modification of TiO 2 nanocomposite PVDF membranes for applications in membrane distillation, J. Membr. Sci., 415 (2012) 850-863.

[32] K. Wang, T. Chung, M. Gryta, Hydrophobic PVDF hollow fiber membranes with narrow pore size distribution and ultra-thin skin for the fresh water production through membrane distillation, Chem. Eng. Sci., 63 (2008) 2587-2594.

[33] P. Todd, S.K. Sikdar, C. Walker, Z.R. Korszun, Application of osmotic dewatering to the controlled crystallization of biological macromolecules and organic compounds, J. Cryst. Growth, 110 (1991) 283-292.

[34] C.-Y. Lee, S.R. McEntyre, P. Todd, K. Schaefer, C.E. Kundrot, Control of nucleation in oligonucleotide crystallization by the osmotic dewatering method with kinetic water removal rate control, J. Cryst. Growth, 187 (1998) 490-498.

[35] W. Ye, J. Wu, F. Ye, H. Zeng, A.T.K. Tran, J. Lin, P. Luis, B. Van der Bruggen, Potential of osmotic membrane crystallization using dense membranes for Na_2CO_3 production in a CO_2 capture scenario, Cryst. Growth Des., 15 (2015) 695-705.

[36] X. Ji, E. Curcio, S. Al Obaidani, G. Di Profio, E. Fontananova, E. Drioli, Membrane distillation-crystallization of seawater reverse osmosis brines, Sep. Purif. Technol., 71 (2010) 76-82.

[37] J.R. McCutcheon, R.L. McGinnis, M. Elimelech, Desalination by ammonia–carbon dioxide forward osmosis: influence of draw and feed solution concentrations on process performance, J. Membr. Sci., 278 (2006) 114-123.

[38] N.Y. Yip, A. Tiraferri, W.A. Phillip, J.D. Schiffman, M. Elimelech, High

performance thin-film composite forward osmosis membrane, Environ. Sci. Technol., 44 (2010) 3812-3818.

[39] Y. Hartanto, S. Yun, B. Jin, S. Dai, Functionalized thermo-responsive microgels for high performance forward osmosis desalination, Water Res., 70 (2015) 385-393.

[40] C. Tang, Y. Zhao, R. Wang, C. Hélix-Nielsen, A. Fane, Desalination by biomimetic aquaporin membranes: Review of status and prospects, Desalination, 308 (2013) 34-40.

[41] C. Tang, Z. Wang, I. Petrinić, A.G. Fane, C. Hélix-Nielsen, Biomimetic aquaporin membranes coming of age, Desalination, (2015). DOI: 10.1016/j.desal.2015.04.026.

[42] H.T. Madsen, N. Bajraktari, C. Hélix-Nielsen, B. Van der Bruggen, E.G. Søgaard, Use of biomimetic forward osmosis membrane for trace organics removal, J. Membr. Sci., 476 (2015) 469-474.

[43] R.C. Ong, T.-S. Chung, J.S. de Wit, B.J. Helmer, Novel cellulose ester substrates for high performance flat-sheet thin-film composite (TFC) forward osmosis (FO) membranes, J. Membr. Sci., 473 (2015) 63-71.

[44] S. Zhang, K.Y. Wang, T.-S. Chung, Y. Jean, H. Chen, Molecular design of the cellulose ester-based forward osmosis membranes for desalination, Chem. Eng. Sci., 66 (2011) 2008-2018.

[45] R.C. Ong, T.-S. Chung, B.J. Helmer, J.S. de Wit, Novel cellulose esters for forward osmosis membranes, Ind. Eng. Chem. Res., 51 (2012) 16135-16145.

[46] S. Zhang, K.Y. Wang, T.-S. Chung, H. Chen, Y. Jean, G. Amy, Well-constructed

cellulose acetate membranes for forward osmosis: minimized internal concentration polarization with an ultra-thin selective layer, J. Membr. Sci., 360 (2010) 522-535.

[47] M. Sairam, E. Sereewatthanawut, K. Li, A. Bismarck, A. Livingston, Method for the preparation of cellulose acetate flat sheet composite membranes for forward osmosis—desalination using $MgSO_4$ draw solution, Desalination, 273 (2011) 299-307.

[48] J. Su, Q. Yang, J.F. Teo, T.-S. Chung, Cellulose acetate nanofiltration hollow fiber membranes for forward osmosis processes, J. Membr. Sci., 355 (2010) 36-44.

[49] Y. Zhao, C. Qiu, X. Li, A. Vararattanavech, W. Shen, J. Torres, C. Helix-Nielsen, R. Wang, X. Hu, A.G. Fane, Synthesis of robust and high-performance aquaporin-based biomimetic membranes by interfacial polymerization-membrane preparation and RO performance characterization, J. Membr. Sci., 423 (2012) 422-428.

[50] J.R. McCutcheon, M. Elimelech, Influence of concentrative and dilutive internal concentration polarization on flux behavior in forward osmosis, J. Membr. Sci., 284 (2006) 237-247.

[51] J. Wei, C. Qiu, C.Y. Tang, R. Wang, A.G. Fane, Synthesis and characterization of flat-sheet thin film composite forward osmosis membranes, J. Membr. Sci., 372 (2011) 292-302.

[52] A. Taubert, Controlling water transport through artificial polymer/protein hybrid membranes, Proc. Natl. Acad. Sci., 104 (2007) 20643-20644.

[53] B.L. de Groot, H. Grubmüller, The dynamics and energetics of water permeation

and proton exclusion in aquaporins, Curr. Opin. Struct. Biol., 15 (2005) 176-183.

[54] J. Ren, J.R. McCutcheon, A new commercial thin film composite membrane for forward osmosis, Desalination, 343 (2014) 187-193.

[55] H. Chen, B. Ilan, Y. Wu, F. Zhu, K. Schulten, G.A. Voth, Charge delocalization in proton channels, I: the aquaporin channels and proton blockage, Biophys. J., 92 (2007) 46-60.

[56] A. Burykin, A. Warshel, What really prevents proton transport through aquaporin? Charge self-energy versus proton wire proposals, Biophys. J., 85 (2003) 3696-3706.

[57] E. Curcio, G. Di Profio, E. Drioli, Membrane crystallization of macromolecular solutions, Desalination, 145 (2002) 173-177.

[58] C.H. Drummond, III 71 st Glass Problems Conference: Ceramic Engineering and Science Proceedings, in, Wiley- American Ceramic Society, Westerville, OH, 2011.

[59] G. Steinhauser, Cleaner production in the Solvay Process: general strategies and recent developments, J. Clean Prod., 16 (2008) 833-841.

Supplementary Material

Click here to download Supplementary Material: Supplementary information.docx

Video Still

Click here to download Video Still: Contact angle of support layer.pptx

Supplementary video

Contact angle of support layer for Aquaporin membrane

Contact angle measurement of support layer.avi